

Engineering of $K_3YSi_2O_7$ To Tune Photoluminescence with Selected Activators and Site Occupancy

Jianwei Qiao,^{†,§} Mahdi Amachraa,^{‡,§} Maxim Molokeev,^{⊥,||,#} Yu-Chun Chuang,[◇] Shyue Ping Ong,^{*,‡,Ⓜ} Qinyuan Zhang,[▽] and Zhiguo Xia^{*,†,▽}

[†]School of Materials Sciences and Engineering, University of Science and Technology Beijing, Beijing 100083, China

[‡]Department of Nanoengineering, University of California, San Diego, 9500 Gilman Drive, La Jolla, California 92093, United States

^{||}Laboratory of Crystal Physics, Kirensky Institute of Physics, Federal Research Center KSC SB RAS, Krasnoyarsk 660036, Russia

[⊥]Siberian Federal University, Krasnoyarsk 660041, Russia

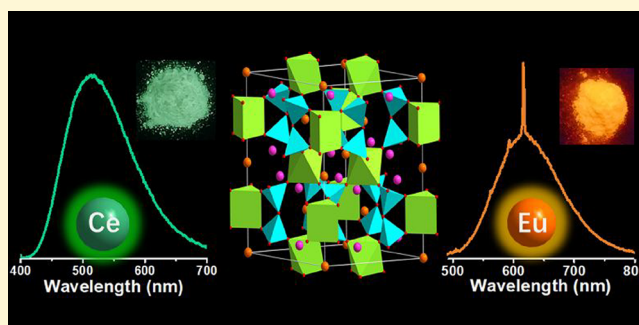
[#]Department of Physics, Far Eastern State Transport University, Khabarovsk 680021, Russia

[◇]National Synchrotron Radiation Research Center, Hsinchu 300, Taiwan

[▽]State Key Laboratory of Luminescent Materials and Devices and Institute of Optical Communication Materials, South China University of Technology, Guangzhou 510641, China

Supporting Information

ABSTRACT: The luminescence of rare earth ions (Eu^{2+} , Ce^{3+} , and Eu^{3+})-doped inorganic solids is attractive for the screening of phosphors applied in solid-state lighting and displays and significant to probe the occupied crystallographic sites in the lattice also offering new routes to photoluminescence tuning. Here, we report on the discovery of the Eu- and Ce-activated $K_3YSi_2O_7$ phosphors. $K_3YSi_2O_7:Eu$ is effectively excited by 450 nm InGaN blue light-emitting diodes (LEDs) and displays an orange-red emission originated from characteristic transitions of both Eu^{2+} and Eu^{3+} , while $K_3YSi_2O_7:Ce^{3+}$ shows green emission upon 394 nm near-ultraviolet (NUV) light excitation. Rietveld refinement verifies the successful doping of the activators, and density functional theory (DFT) calculations further support that Eu^{2+} occupies both K1 and Y2 crystallographic sites, while Ce^{3+} and Eu^{3+} only occupy the Y2 site; hence, the broad-band red emission of Eu^{2+} are attributed to a small DFT band gap (3.69 eV) of $K_3YSi_2O_7$ host and a selective occupancy of Eu^{2+} in a highly distorted K1 site and a high crystal field splitting around Y2 sites. The white LEDs device utilizing orange-red-emitting $K_3YSi_2O_7:Eu$ and green-emitting $K_3YSi_2O_7:Ce^{3+}$ exhibits an excellent CRI of 90.1 at a correlated color temperature of 4523 K. Our work aims at bridging multivalent Eu^{2+}/Eu^{3+} and Ce^{3+} site occupancy in the same host to realize photoluminescence tuning and especially exposes new ways to explore new phosphors with multicolor emission pumped by blue and NUV light for white LEDs.



INTRODUCTION

The tremendous success of phosphor-converted white light-emitting diodes (pc-WLEDs) has led to an in-depth exploration of inorganic solid-state phosphors activated by rare earth ions (e.g., Eu^{2+} , Ce^{3+} , and Eu^{3+}) or transition metal ions (e.g., Mn^{2+} , Mn^{4+} , and Bi^{3+}).^{1–6} Most commercialized pc-WLEDs are produced by combining the yellow-emitting $Y_3Al_5O_{12}:Ce^{3+}$ phosphor with a blue InGaN LED chip, which suffers from a poor rendering index ($R_a < 80$) and high correlated color temperature ($CCT > 4500$ K) due to the lack of red components.^{7,8} Efforts have been made to discover red phosphors which are crucial to achieve illumination-grade lighting ($CCT = 2700–4000$ K, $R_a > 90$).^{9,10} Presently, nitride and fluoride phosphors such as $Sr_2Si_3N_8:Eu^{2+}$, $CaAlSiN_3:Eu^{2+}$, $Sr[LiAl_3N_4]:Eu^{2+}$, $K_2TiF_6:Mn^{4+}$, and $K_2SiF_6:Mn^{4+}$ gave excellent red emission upon blue excitation and have been

applied in high-quality pc-WLEDs.^{10–15} Nevertheless, the harsh synthesis conditions (high temperature/high pressure) for nitride phosphors push up the cost for daily uses, and the massive evaporation of HF gas during the production process and unstable property of fluoride phosphors also hinder their applications.¹⁶ By contrast, oxide-based phosphors with versatile crystal structures possess environmentally friendly and low-cost advantages during the preparation, as well as high chemical stability for the applications. Therefore, discovering new orange-red-emitting oxide-based phosphors, especially pumped by the blue light (445–465 nm), is not only highly

Received: July 26, 2019

Revised: August 13, 2019

Published: August 13, 2019

desirable for warm WLEDs but also represents substantial scientific progress unveiling the limitations of oxide phosphors.

The Ce^{3+} and Eu^{2+} ions possessing f–d electron configurations have been considered as good activators in phosphors due to their broad excitation/emission bands and their luminescence tunability by locally modifying host compositions and structures. However, localization of activators in phosphors is an important but difficult work, and it can hardly be resolved by an experimental way only. Free Ce^{3+} and Eu^{2+} ions have a large energy gap between the 4f ground state and the 5d excited state: 4.2 eV ($34\,000\text{ cm}^{-1}$) for Eu^{2+} ions and 6.2 eV ($50\,000\text{ cm}^{-1}$) for Ce^{3+} .¹⁷ Accordingly, Eu^{2+} ions usually exhibit a red-shifted emission compared to Ce^{3+} ions when introduced in the same host lattice.¹ If Ce^{3+} and Eu^{2+} are properly engineered in a host, tunable photoluminescence and even white light emission can be achieved. As one of the most commonly used red emission activators, Eu^{3+} ions mainly exhibit a characteristic parity-forbidden 4f–4f transitions resulting from the $^5\text{D}_0$ – $^7\text{F}_J$ ($J = 0, \dots, 4$) transitions. Mixed valency of Eu^{2+} and Eu^{3+} has been observed in some hosts, such as BaMgSiO_4 , $\text{CsAlSi}_2\text{O}_6$, CaYAlO_4 , SrAl_3BO_7 , and so on.^{18–21} In particular, $\text{SrAl}_2\text{O}_4:\text{Eu}$ realize tunable emission from red to yellow by controlling the reduction of dopants, and $\text{K}_3\text{YSi}_2\text{O}_7:\text{Dy}$, Eu achieves white light emission with multivalent Eu and Dy^{3+} .^{22–24} However, limited research has been conducted on the site occupation of Eu^{2+} and Eu^{3+} . Moreover, the emission peaks of Eu^{2+} in these phosphors are usually located in the bluish-green region. Understanding the crystallographic site occupation of Eu^{2+} and Eu^{3+} is paramount because their luminescence properties are directly related to their local environment.

Another challenge in exploring phosphors for pc-WLEDs is to reduce the energy gap between the 4f level and the lowest 5d level to below 3.1 eV (400 nm) to match the emission of InGaN LED chips.²⁵ This energy gap requirement demands for scientists to explore new oxide host crystals with shorter activator–anion bond lengths and high polyhedral distortion.²⁶ The band gap E_g also plays an essential role in the emission wavelength as the conduction band character of the host affects the excited energy level of the phosphor.²⁷ Computationally, Wang et al. found that the Perdew–Burke–Ernzerhof (PBE) band gap is inversely correlated with the emission wavelength with a small PBE band gap of between 2.42 and 3.58 eV corresponding to red emission in Eu^{2+} -activated phosphors.²⁶ In theory, finding a new red-emitting oxide phosphor may be feasible by targeting hosts with smaller PBE band gaps.

Recently, the design principle on the discovery of Eu^{2+} -doped oxide-based red-emitting phosphors has been proposed by our group, thanks to the activators' site occupation located in a polyhedra with small coordination numbers, and thus, $\text{Rb}_3\text{YSi}_2\text{O}_7:\text{Eu}^{2+}$ was reported to show broad-band red emission peaking at 622 nm under 450 nm blue light excitation.²⁸ In this work, novel orange-red-emitting $\text{K}_3\text{YSi}_2\text{O}_7:\text{Eu}^{2+}/\text{Eu}^{3+}$ phosphor excited by blue light (450 nm) and green-emitting $\text{K}_3\text{YSi}_2\text{O}_7:\text{Ce}^{3+}$ phosphor pumped by near-ultraviolet (NUV) light (394 nm) have been discovered; in particular, the crystal structure of $\text{K}_3\text{YSi}_2\text{O}_7$ is different from that previously reported for $\text{Rb}_3\text{YSi}_2\text{O}_7$. It is found that the coexistence of Eu^{3+} and Eu^{2+} in $\text{K}_3\text{YSi}_2\text{O}_7$ host introduces the Eu^{3+} additional red components (622 nm) into the already broad emission band of Eu^{2+} (620 nm). Moreover, under the excitation of NUV (394 nm) light, Ce^{3+} -activated $\text{K}_3\text{YSi}_2\text{O}_7$ phosphor shows a broad green emission band peaking at 514

nm. We provide detailed insights into the photoluminescence properties, electronic properties, and sites preference for $\text{Eu}^{2+}/\text{Eu}^{3+}$ and Ce^{3+} ions in $\text{K}_3\text{YSi}_2\text{O}_7$ using density functional theory (DFT) calculations. A prototype pc-WLEDs utilizing $\text{K}_3\text{YSi}_2\text{O}_7:\text{Eu}^{2+/3+}$ and $\text{K}_3\text{YSi}_2\text{O}_7:\text{Ce}^{3+}$ yields an excellent CRI of >90. Our research also aims at initiating novel discoveries of new oxide-based red phosphor and to help better the understanding of the site's occupation of multivalent $\text{Eu}^{2+}/\text{Eu}^{3+}$ and Ce^{3+} site occupancy in the same host to realize photoluminescence tuning toward the targeted application in white LEDs.

■ EXPERIMENTAL SECTION

Synthesis. Pure phased Eu^{2+} , Eu^{3+} , and Ce^{3+} -doped $\text{K}_3\text{YSi}_2\text{O}_7$ phosphors were prepared by the conventional high-temperature solid-state reaction. According to the given compositions, the stoichiometry contents of raw materials K_2CO_3 , Y_2O_3 , SiO_2 , Eu_2O_3 , and CeO_2 were weighed and ground in an agate about 1 h for full mixing. The resulting mixtures were sintered at 1250 °C for 8 h in a reducing mixed atmosphere of H_2 (10%) and N_2 (90%) and then cooled to room temperature. The sintered samples were ground again for subsequent measurements.

Characterization. Powder XRD patterns were recorded by a D8 ADVANCE Bruker diffractometer (Cu $K\alpha$ radiation; $\lambda = 1.5418\text{ \AA}$) operating at 40 kV and 40 mA. Synchrotron XRD (SXRD) patterns were determined at TPS 09A (Taiwan Photon Source) of the National Synchrotron Radiation Research Center with a calibrated wavelength of 0.82656 Å. Rietveld analysis of the synchrotron XRD was done using the TOPAS 4.2. program.²⁹ The morphologies were examined by scanning electron microscopy (SEM, JEOL JSM-6510A). The X-ray absorption near-edge structure (XANES) of the Eu L3 edge was recorded on the beamline of 1W1B at the Beijing Synchrotron Radiation Facility. Photoluminescence excitation (PLE) and emission (PL) spectra were measured by an Edinburgh FLSP-920 fluorescence spectrometer equipped with both continuous (450 W) and xenon (Xe) lamps. Temperature-dependent PL spectra were measured from 300 to 500 K by FLSP-920 connected with heating equipment. Decay curves were performed by FLSP-920 equipped with a microsecond pulsed Xe lamp and a nF900 flash lamp as the excitation source. Two different types of WLEDs were fabricated based on a NUV chip ($\lambda_{\text{max}} = 395\text{ nm}$) and a blue chip ($\lambda_{\text{max}} = 455\text{ nm}$) encapsulated in translucent resin containing various phosphors. The color temperature (CT) and the color rendering index (CRI) as well as the photoluminescence spectra were collected by using an integrating sphere spectroradiometer system (ATA-1000, Ever fine).

■ COMPUTATIONAL METHODOLOGY

Structural Relaxation of Hosts. All density functional calculations were performed using the Vienna ab initio simulation package (VASP) within the projector-augmented wave method.^{30,31} Generalized gradient approximation PBE functionals for structure relaxation were used. The plane wave energy cutoff was 520 eV, and the Brillouin zones were integrated with a k -point grid density of at least 100 per \AA^{-3} (reciprocal lattice volume). Parameters conforming to the Materials Project were utilized to carry out all properties calculations for host materials, such as energy, and band structure calculations.³² Moreover, all crystal manipulations and data analysis were carried out by using the Python Material Genomics package.³³

Structural Relaxation of Doped Hosts. For calculations of $\text{Eu}^{2+}/\text{Eu}^{3+}/\text{Ce}^{3+}$ -activated phosphors, we used the PBE+U method with a Hubbard U value of 2.5 eV.³⁴ Supercell models of at least 10 Å on each lattice parameter were adopted to simulate the low concentration of Eu concentration in an experimental setting. Structures are entirely relaxed with

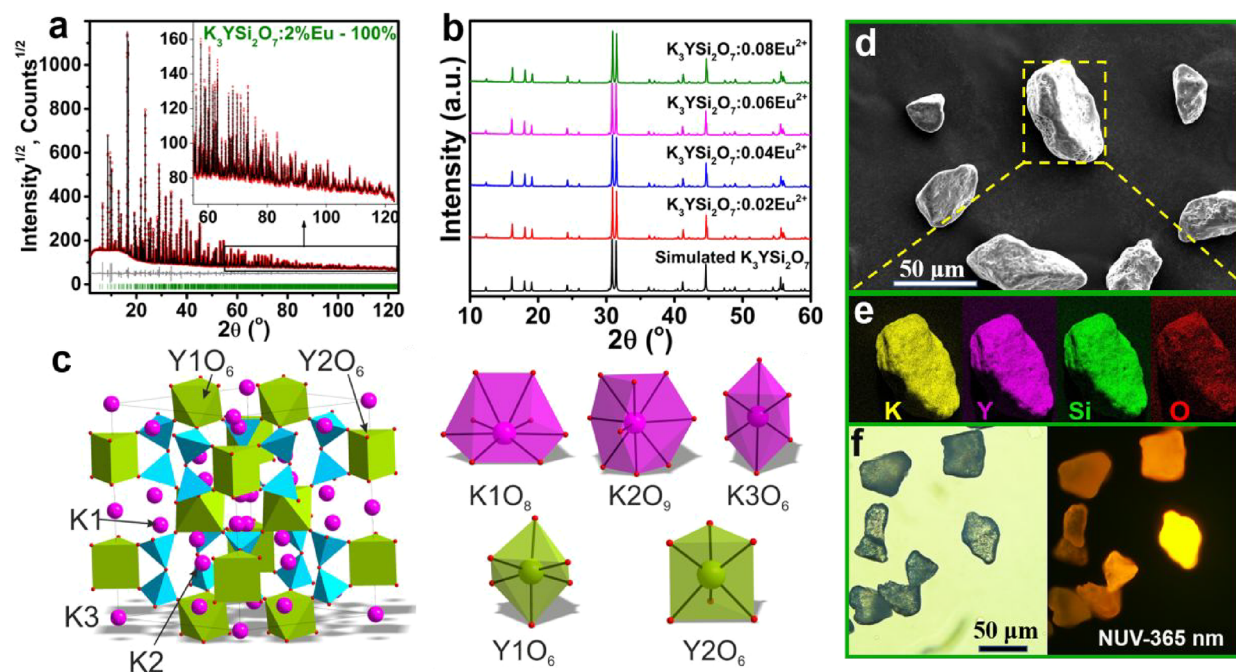


Figure 1. (a) Synchrotron X-ray powder diffraction of $\text{K}_3\text{YSi}_2\text{O}_7:0.02\text{Eu}$ with the measured data and calculated profile based on Rietveld refinement. (b) Simulated and measured XRD patterns of $\text{K}_3\text{YSi}_2\text{O}_7:x\text{Eu}$ ($x = 0.02-0.08$) and $\text{K}_3\text{YSi}_2\text{O}_7:0.02\text{Ce}$. (c) Crystal structure of $\text{K}_3\text{YSi}_2\text{O}_7$ obtained by Rietveld refinement and the coordinate environments of K1, K2, K3, Y1, and Y2 sites. (d) SEM images of $\text{K}_3\text{YSi}_2\text{O}_7:\text{Eu}$ particles. (e) EDS mapping of K, Y, Si, and O elements in $\text{K}_3\text{YSi}_2\text{O}_7:\text{Eu}$. (f) Optical microscope photographs of the $\text{K}_3\text{YSi}_2\text{O}_7:\text{Eu}$ microcrystal particles without (left) and with (right) NUV-365 nm excitation.

energies and forces converged to within 10^{-5} eV and 0.01 eV \AA^{-1} , respectively.

Defect formation energies were calculated using the Wei et al formalism:³⁵

$$E_f = E_{\text{tot}}^{\text{D}} - E_{\text{tot}}^{\text{B}} - \sum_i n_i \mu_i$$

where $E_{\text{tot}}^{\text{D}}$ and $E_{\text{tot}}^{\text{B}}$ are the total energies of the structure with and without the defect(s), respectively, μ_i is defined as the atomic chemical potential of species i , and n_i indicates the number of atoms of species i being removed ($n_i < 0$) or added ($n_i > 0$). Finally, μ_i is determined based on the chemical potentials for each species based on the 0 K DFT phase diagram.

Local Environment Analysis. An advanced and robust local environment assessment algorithm implemented in pymatgen is used.³⁶ Moreover, Hoppe's effective coordination number (ECoN) is utilized to include a geometrical bond weight.³⁷

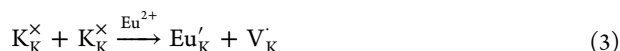
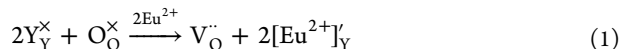
RESULTS AND DISCUSSION

Crystal Structure and Site Occupations of Eu^{2+} , Eu^{3+} , and Ce^{3+} . The crystal structure of $\text{K}_3\text{YSi}_2\text{O}_7:x\text{Eu}$ ($x = 0.02, 0.06, 0.08$) at room temperature was refined using a Rietveld analysis for the diffraction data from a synchrotron device ($\lambda = 0.82656$ \AA radiation) and 1D MYTHEN 24K detector. Powder diffraction data were collected for the samples with two different Eu concentrations (0.02 and 0.06), were identically indexed, and correspond to a hexagonal cell ($P6_3/mcm$), and the structural parameters were found to be close to those of the $\text{K}_3\text{YSi}_2\text{O}_7$ crystal (Figure 1a and Figure S1).²³ Minor impurity phases of Y_2O_3 were found at an activator's concentration of 0.08 (wt $\approx 0.62(2)\%$) (Figure S1b). Rietveld refinement performed using TOPAS 4.2 was conducted on $\text{K}_3\text{YSi}_2\text{O}_7:x\text{Eu}$

for the three concentrations mentioned above. All refinements were reliable and stable with low R factors (Table S1). Coordinates of atoms and main bond lengths are given in Tables S2 and S3, respectively. Figure 1b depicts the measured and simulated XRD patterns of the host, $\text{K}_3\text{YSi}_2\text{O}_7:x\text{Eu}$ ($x = 0.02-0.08$) and $\text{K}_3\text{YSi}_2\text{O}_7:0.02\text{Ce}$ phosphors. All of the diffraction peaks of $\text{K}_3\text{YSi}_2\text{O}_7:x\text{Eu}$ are well indexed to the $P6_3/mcm$ space group, and no prominent impurity peaks were observed. The Eu ions can potentially locate in K and Y sites of the host. The cell volume increasing with x (Figure S1c) indicates that the Eu ions should mainly occupy Y^{3+} sites since Eu^{2+} and Eu^{3+} ions are bigger than the Y^{3+} ion and smaller than K^+ . Also, some part of the Eu ions can be also located in K^+ sites. Scanning electron microscope (SEM) images of the as-synthesized powders (Figure 1d) reveal good crystallization at the micrometer scale. The optical microscope photographs (Figure 1f) of $\text{K}_3\text{YSi}_2\text{O}_7:x\text{Eu}$ phosphors further demonstrate that the particles are effectively in the micrometer range, and an orange-red emission under 365 nm can be observed. Moreover, element mapping images (Figure 1e) reflect that K, Y, Si, and O elements are homogeneously distributed within the $\text{K}_3\text{YSi}_2\text{O}_7$ particles.

In the $\text{K}_3\text{YSi}_2\text{O}_7$ host (Figure 1c) there are three symmetrically distinct K sites with 8-fold (K1), 9-fold (K2), and 6-fold (K3) coordination and two symmetrically distinct Y sites with 6-fold coordination. (Y1 and Y2). K1 offers the largest average bond length and also the most distorted environment, while the K3 octahedron site has the smallest average bond length (2.77 \AA) and also the least distorted environment (Table S4). The average bond lengths of Y1 and Y2 are 2.31 and 2.27 \AA , respectively. Unfortunately, Eu and Ce concentrations throughout the samples were too low to allow refinement and hence site identification. Figure S1c shows the cell volumes of $\text{K}_3\text{YSi}_2\text{O}_7:x\text{Eu}$ ($x = 0.02, 0.06, 0.08$) increase

with the x values, indicating that Eu atoms are inserted in some cationic sites with small radii, thus leading to a lattice expansion. We performed DFT calculations on Eu^{2+} , Eu^{3+} , and Ce^{3+} -activated $\text{K}_3\text{YSi}_2\text{O}_7$ using a $2 \times 2 \times 1$ supercell (24 formula units). For aliovalent Eu^{2+} activation, we comprehensively evaluated by DFT three charge-neutral defect configurations



We find that the $2\text{Y}_Y^\times + \text{O}_O^\times$ defect combination (using Kröger-Vink notation) has the highest dopant formation, 9.382 eV per formula unit (fu), while $\text{K}_K^\times + \text{Y}_Y^\times$ has a dopant formation energy of 0.962 eV/fu. As stated above, there exist 3 symmetrically distinct sites for K^+ and 2 symmetrically distinct sites for Y^{3+} . After considering all of the possible charge-neutral configurations within scenario 2 and computing all possible dopant formation energies (Figure 2a), it was found that Eu^{2+}

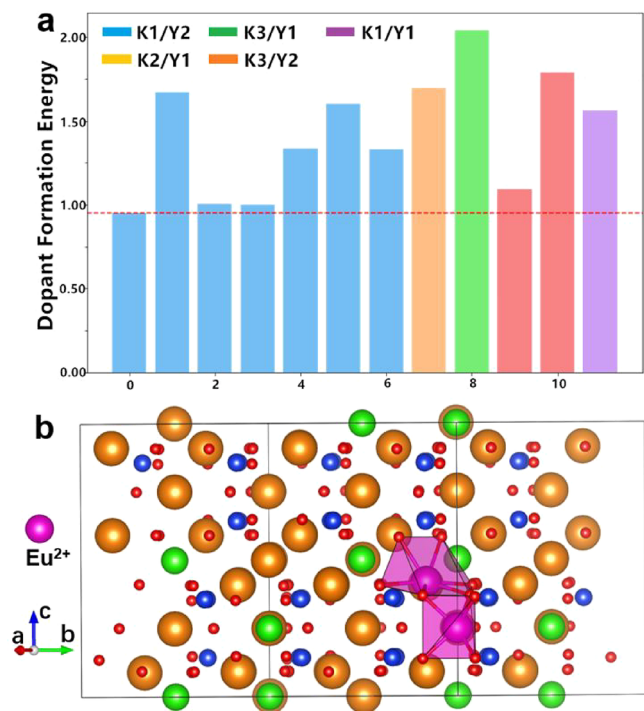


Figure 2. (a) Formation energies of Eu^{2+} ions entering K1/Y2, K2/Y1, K3/Y2, and K1/Y1 sites. (b) Site occupation of Eu^{2+} ions in the $\text{K}_3\text{YSi}_2\text{O}_7$: Eu^{2+} crystal structure.

occupies K1 with an average bond length of 2.78 Å and Y2 with an average bond length of 2.49 Å. The occupation of Eu^{2+} in a polyhedron with a small bond length leads to a large crystal field splitting of Eu^{2+} 5d levels and thus should result in a red-shifted emission. Furthermore, the two introduced Eu^{2+} in $\text{K}_3\text{YSi}_2\text{O}_7$ are corner sharing two oxygens, and the Eu^{2+} – Eu^{2+} interactivator distance is about 4.1 Å (Figure 2b). Hence, we conclude that introduction of Eu^{2+} in $\text{K}_3\text{YSi}_2\text{O}_7$ is likely to be charge compensated by Eu^{2+} occupying both K^+ and Y^{3+} . For scenario 3 the dopant formation energy was found to be 0.561 eV/fu and is the lowest dopant formation energy among

all 3 possible aliovalent substitutions. It was found that Eu^{2+} occupies the K1 site with an average bond length of 2.81 Å. Moreover, it was found that the K vacancy formed on a K1 site as well. Since both scenarios 2 and 3 have relatively small dopant formation energies, it is assumed that both configurations are possible. For Ce^{3+} site occupation within $\text{K}_3\text{YSi}_2\text{O}_7$ host, DFT calculations again revealed that Ce^{3+} activator prefers the Y2 site (trigonal prism) more than the Y1 site (octahedron) by about 95 meV. The Ce^{3+} local environment remains a trigonal prism, with an increased average bond length from 2.31 to 2.40 Å. It is also found that Eu^{3+} prefers to sit on the Y2 site (trigonal prism) with an average bond length of 2.37 Å. The energy difference between the two Y sites is about 260 meV.

Photoluminescence Properties. The inset of Figure 3a shows that the representative $\text{K}_3\text{YSi}_2\text{O}_7$:0.04Eu phosphor displays a pale-yellow color under natural light illumination and a bright orange-red-light emission color under NUV light (365 nm) excitation. The normalized PL and PLE spectra of $\text{K}_3\text{YSi}_2\text{O}_7$:0.04Eu measured at room temperature are shown in Figure 3a. Under a 450 nm excitation, the emission spectrum displays a broad-band emission from 500 to 750 nm attributed to the available $4f^65d^1 \rightarrow 4f^7$ transition energies of Eu^{2+} . However, typical sharp line emission attributed this time to $^5\text{D}_0 \rightarrow ^7\text{F}_J$ ($J = 0, 1, 2, 3, 4$) transition energies of Eu^{3+} were also detected under a 450 nm excitation. The excitation spectrum monitored at 620 nm also shows a broad-band character from 250 to 500 nm including a few sharp lines (such as 394 nm); these sharp lines are ascribed to Eu^{3+} ($4f^6$) $^5\text{D}_0 \rightarrow (4f^6)^7\text{F}_2$ transition energies, suggesting the coexistence of Eu^{2+} and Eu^{3+} in the lattice. The PL and PLE spectra for several Eu doping concentrations are shown in Figure S2a and S2b. An increase of Eu concentration increases the emission intensity of Eu^{2+} with an observed maximum intensity when $x = 0.04$; beyond a 0.04 Eu concentration, the intensity starts to decrease. The emission intensity from Eu^{3+} shows a continued increase and hence a different concentration quenching behavior. In fact, Eu^{2+} and Eu^{3+} should theoretically have different concentration quenching sensitivity, and the observation from Figure S2a and S2b is explicit. Furthermore, the PL/PLE results of $\text{K}_3\text{YSi}_2\text{O}_7$: $x\text{Eu}$ ($x = 0.02$ – 0.08) are similar, and all of them distinguishably exhibit the Eu^{2+} and Eu^{3+} emission/excitation peaks, confirming their respective coexistence in $\text{K}_3\text{YSi}_2\text{O}_7$:Eu phosphors. X-ray absorption near-edge structure (XANES) measurements further certify the mixed-valency coexistence. Eu-L3 edge spectra for $\text{K}_3\text{YSi}_2\text{O}_7$: $x\text{Eu}$ ($x = 0.02, 0.04, 0.08$) are measured and shown in Figure 3b. The two peaks at 6974 and 6983 eV are ascribed to the $2p_{3/2} \rightarrow 5d$ transition of Eu^{2+} and Eu^{3+} , respectively.³⁸ The relative intensity of Eu^{3+} in XANES spectrum is stronger than that of Eu^{2+} , reflecting a higher Eu^{3+} content in $\text{K}_3\text{YSi}_2\text{O}_7$:Eu phosphors.³⁹ However, Eu^{2+} belongs to a spin- and parity-allowed transition, and one can still find strong broad-band $5d \rightarrow 4f$ emission.⁴⁰ For Ce^{3+} -activated $\text{K}_3\text{YSi}_2\text{O}_7$, the excitation spectrum monitored at 514 nm shows two narrow band peaks at 329 and 390 nm (Figure 3c), which are both attributed to $4f^1 \rightarrow 4f^05d^1$ transition energies of Ce^{3+} ions. Besides, under a 394 nm excitation, $\text{K}_3\text{YSi}_2\text{O}_7$:0.02 Ce^{3+} phosphor exhibits a broad green-emitting centered at 514 nm. Figure 3c shows photographs of $\text{K}_3\text{YSi}_2\text{O}_7$:0.02Ce phosphor under natural light and NUV (365 nm) excitation.

The measured broad emission band of Eu^{2+} (Figure S3a) can be decomposed into two Gaussian curves peaks centered at 16 766 (596 nm) and 15 571 cm^{-1} (642 nm), suggesting the

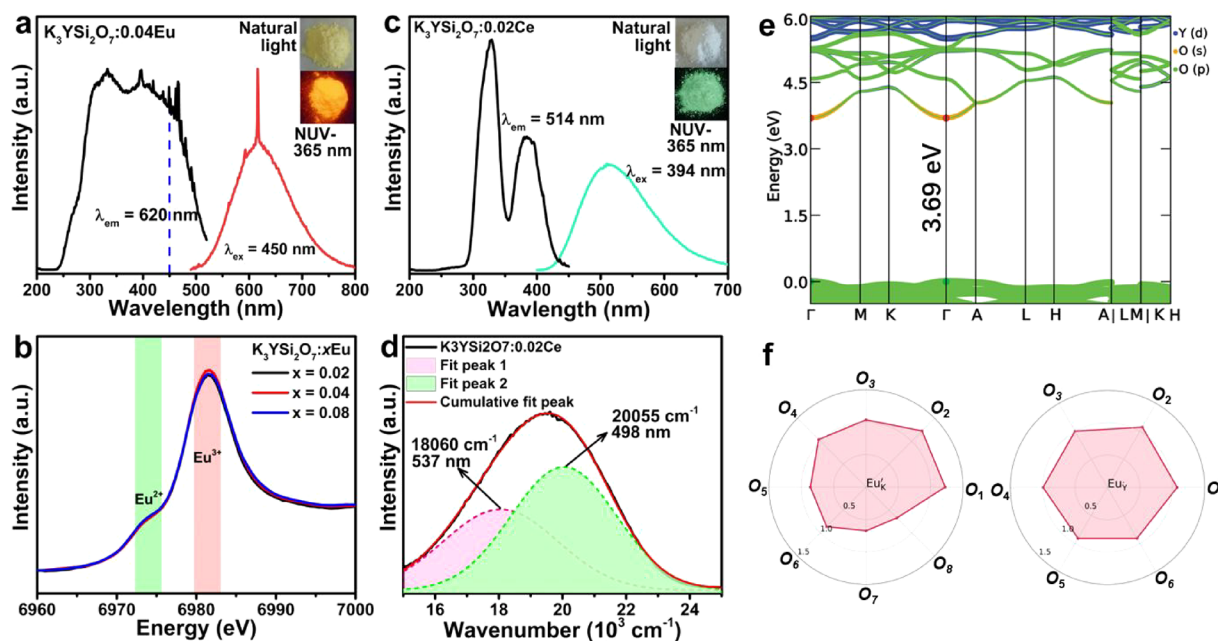


Figure 3. (a) Excitation ($\lambda_{em} = 620$ nm) and emission ($\lambda_{ex} = 450$ nm) spectra at room temperature of $K_3YSi_2O_7:0.04Eu$; (inset) images of $K_3YSi_2O_7:0.04Eu$ powders under natural light illumination and NUV-365 nm excitation. (b) X-ray absorption near-edge structure (XANES) spectra of the Eu L3 edge in $K_3YSi_2O_7:xEu$ ($x = 0.02, 0.04, 0.08$). (c) Excitation ($\lambda_{em} = 514$ nm) and emission ($\lambda_{ex} = 394$ nm) spectra at room temperature of $K_3YSi_2O_7:0.02Ce$. (d) Gaussian fitting curves of the $K_3YSi_2O_7:0.02Ce$ emission spectrum. (e) Band structure of $K_3YSi_2O_7$ host. (f) Eu^{2+} ligands' bond weights in $K_3YSi_2O_7$ (Note: both graphs are plotted within the same radius range).

existence of the two emission centers. Moreover, when monitored at 620 nm, the lifetimes (Figure S3b, Table S5) are well fitted to a decay model obeying a double-exponential function with an average lifetime of 2.47 μ s. Consequently, these results agree well with those of the DFT calculations, where Eu^{2+} is predicted to occupy both K1 and Y2 sites in $K_3YSi_2O_7$ host. As stated earlier, Eu^{2+} occupying the Y2 site experiences a smaller average bond length, which is expected to lead to a larger crystal field splitting in the 5d levels of Eu^{2+} . For Ce^{3+} -activated $K_3YSi_2O_7$, the broad emission band is decomposed into two Gaussian curves with maxima at 20 055 (498 nm) and 18 060 cm^{-1} (537 nm) (Figure 3d), which generally are attributed to ${}^2D_{3/2} \rightarrow {}^2F_{5/2}$ and ${}^2D_{3/2} \rightarrow {}^2F_{7/2}$ spin-orbit coupled transitions in Ce^{3+} .⁴¹ Despite the presence of two Gaussian fitting curves, the energy difference between 498 and 537 nm is 1995 cm^{-1} (~ 3.1 eV), which is in the vicinity of the theoretical value of Ce^{3+} (2000 cm^{-1}), suggesting the single emission center in this host.⁴² Decay curves of $K_3YSi_2O_7:0.02Ce$ monitored at 514 nm can be also well fitted by a single-exponential function with a decay time of about 44.23 ns (Figure S3c), which further substantiates that Ce^{3+} only occupies a single crystallographic site in $K_3YSi_2O_7$ host. DFT calculations likewise corroborate that Ce^{3+} prefers to occupy Y2 rather than Y1 by 95 meV.

Emission energies are known to be related to the host material band gap E_g ; the minimum conduction band of the host material sets the energy level of the excited Eu^{2+} -activated phosphor. Wang et al. reveal that red-emitting phosphors usually have a relatively small Perdew–Burke–Ernzerhof (PBE) E_g with a range of 2.42–3.58 eV. The DFT-calculated band gap of $K_3YSi_2O_7$ using the PBE functional is 3.69 eV (Figure 3e), suggesting that it has a high possibility to yield an orange-red emission when activated with Eu^{2+} . On the other hand, Eu^{2+}/Ce^{3+} emission properties are highly dependent on their respective crystal field splitting, which in return is mainly

related to the activators' local environment. However, due to the inherent nature of Eu^{3+} transitions, the emission spectrum can hardly be shifted or modified and usually has a typical emission at 610 nm as observed in Figure 3a. The Gaussian decomposition of the $K_3YSi_2O_7:0.04Eu$ emission spectrum and the room-temperature decay curve monitored at 620 nm indisputably revealed the presence of two Eu^{2+} emission centers and a single Eu^{3+} emission center (sharp peak).

We may identify the Eu^{2+} site responsible for each emission peak by considering the activator local environment. The bond weight distribution of Eu^{2+} in $K_3YSi_2O_7$ is calculated and shown in Figure 3f. Eu^{2+} on Y2 site shows relatively the same bond weight for all of their oxygen ligands, while Eu^{2+} on K1 site shows a discrepancy in its oxygen bond weights. By only considering the highest bond weights around Eu^{2+} on K1, both Y2 and K1 sites are assumed to be 6-fold coordinated (trigonal prism). However, Eu^{2+} in the Y2 site has a shorter average bond length (2.49 Å) and a less distorted coordination polyhedron, while Eu^{2+} in the K1 site has a larger average bond length (2.78 Å) and more distorted coordination polyhedron (Table S4). The crystal field splitting rapidly decreases with increases in the distances between the central activator atom and the surrounding ligands. Hence, a smaller average bond length in the Y2 site is responsible for the lower emission energy (642 nm) peak, and a larger average bond length in K1 site is matched with the higher energy emission (596 nm) peak as reported in Figure S3a. Furthermore, in low-symmetry distorted sites such as the K1 site, the 5d orbitals of Eu^{2+} are resolved into additional energy levels where at least one of the lower levels is further stabilized.⁴³ Therefore, the large bandwidth emission around the red region is ascribed to a highly distorted K1 site. Moreover, the presence of a K vacancy induces additional distortions around Eu^{2+} on K1 and further amplifies the broad-band character.

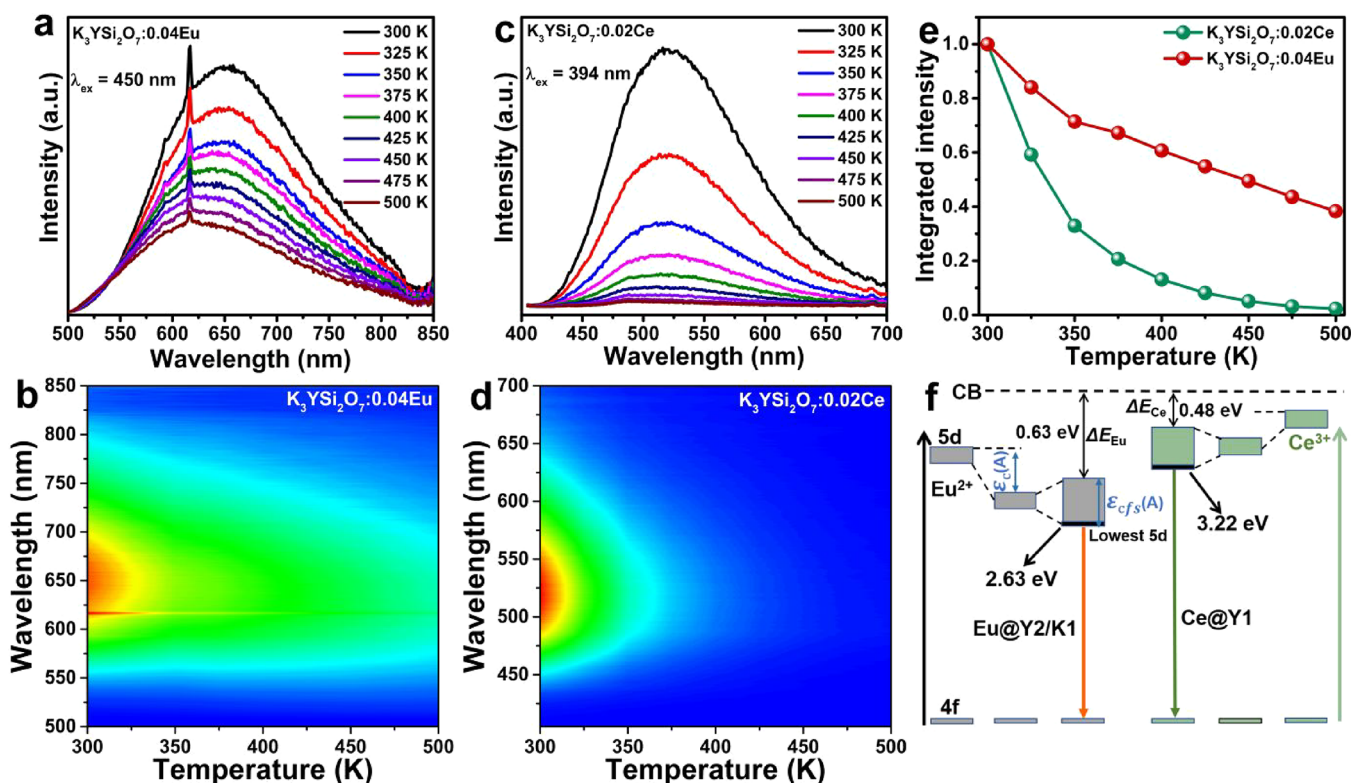


Figure 4. (a and b) Temperature-dependent emission spectra of $\text{K}_3\text{YSi}_2\text{O}_7:0.04\text{Eu}$ in the temperature range of 300–500 K. (c and d) Temperature-dependent emission spectra of $\text{K}_3\text{YSi}_2\text{O}_7:0.02\text{Ce}$ in the temperature range of 300–500 K. (e) Temperature-dependent integrated emission intensity of $\text{K}_3\text{YSi}_2\text{O}_7:0.04\text{Eu}$ and $\text{K}_3\text{YSi}_2\text{O}_7:0.02\text{Ce}$. (f) Schematic energy level diagram for $\text{Eu}^{2+}/\text{Ce}^{3+}$ ions in the $\text{K}_3\text{YSi}_2\text{O}_7$ host crystal structure.

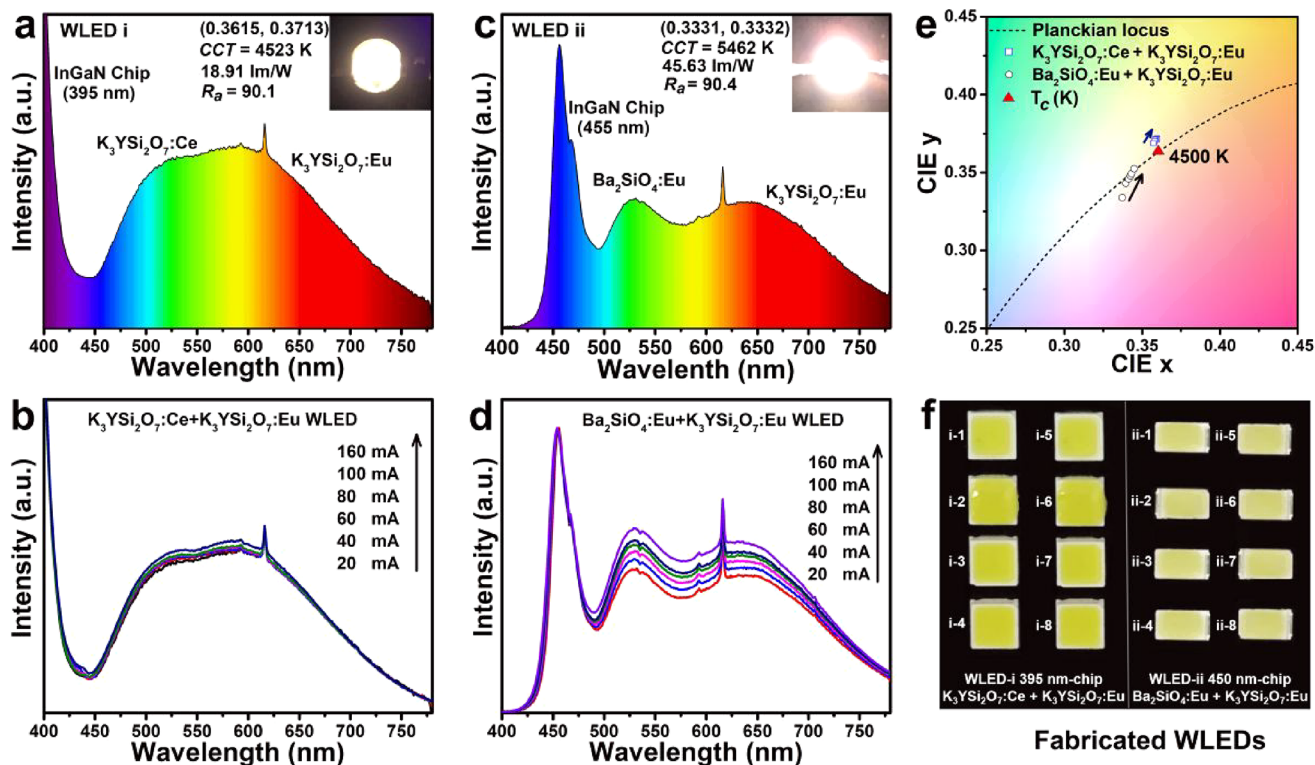


Figure 5. (a and b) Photograph and PL spectra of the fabricated WLED based on InGaN ($\lambda_{\text{max}} = 395$ nm) + $\text{K}_3\text{YSi}_2\text{O}_7:0.02\text{Ce} + \text{K}_3\text{YSi}_2\text{O}_7:0.04\text{Eu}$ phosphor (WLED i). (c and d) Photograph and PL spectra of the fabricated WLED based on InGaN ($\lambda_{\text{max}} = 455$ nm) + $\text{Ba}_2\text{SiO}_4:\text{Eu} + \text{K}_3\text{YSi}_2\text{O}_7:0.04\text{Eu}$ phosphor (WLED ii). (e) Chromaticity coordinates of the fabricated WLEDs under various forward bias currents. (f) Photograph of two different types of WLEDs. (Note: WLEDs of i-1–8 are packaged with different mass ratios of $\text{K}_3\text{YSi}_2\text{O}_7:0.02\text{Ce}$ and $\text{K}_3\text{YSi}_2\text{O}_7:0.04\text{Eu}$ phosphors, and ii-1–8 are packaged with different mass ratios of $\text{Ba}_2\text{SiO}_4:\text{Eu}$ and $\text{K}_3\text{YSi}_2\text{O}_7:0.04\text{Eu}$ phosphors.)

Thermal Quenching Properties. The thermal stability is another important criterion in evaluating a potential phosphor for WLED application. The emission intensities of $\text{K}_3\text{YSi}_2\text{O}_7:0.04\text{Eu}$ and $\text{K}_3\text{YSi}_2\text{O}_7:0.02\text{Ce}$ phosphor excited by 450 nm blue light and 394 nm NUV light were investigated as a function of temperature in the range from 300 to 500 K, respectively, as shown in Figure 4a and 4b and Figure 4c and 4d. Unsurprisingly, emission intensity of both $\text{Eu}^{2+}/\text{Eu}^{3+}$ and Ce^{3+} decreases with increasing of temperature, and only about 49% and 5% emission intensity remains at 425 K (Figure 4e) for $\text{K}_3\text{YSi}_2\text{O}_7:0.04\text{Eu}$ and $\text{K}_3\text{YSi}_2\text{O}_7:0.02\text{Ce}$ phosphor, respectively. Also, $\text{K}_3\text{YSi}_2\text{O}_7:0.02\text{Ce}$ shows a more rapid quenching process than that of $\text{K}_3\text{YSi}_2\text{O}_7:0.04\text{Eu}$. Two models have commonly addressed the thermal quenching process.⁴⁴ On one hand, a nonradiative relaxation model suggests that substantial atomic geometry changes lead to the crossing of the Eu_{5d} and Eu_{4f} configurational energy curves.⁴⁵ On the other hand, Dorenbos suggested a model where the thermal excitation of electrons from the Eu_{5d} level to the conduction band minimum (CBM) leads to an autoionization process.⁴⁶ On the basis of Dorenbos's model, the smallest the gap between the Eu_{5d} -CBM the greater the thermal quenching. Our experimental thermal quenching measurements inferred that the auto-ionization model is the most likely model to be occurring. The $\text{K}_3\text{YSi}_2\text{O}_7$ host band gap was computationally found to be small; moreover, the emission energies of the Eu^{2+} - and Ce^{3+} -activated host ultimately suggested that $\text{K}_3\text{YSi}_2\text{O}_7:0.04\text{Eu}$ would endure less thermal quenching than $\text{K}_3\text{YSi}_2\text{O}_7:0.02\text{Ce}$ phosphor as shown in Figure 4f. Dorenbos's model empirically defines a formula to appraise the value of the Eu_{5d} -CBM gap, also denominated as the thermal quenching barrier ΔE . The latter can be derived from the following empirical formula²⁷

$$\Delta E = \frac{T_{0.5}}{680} \text{ eV} \quad (1a)$$

where $T_{0.5}$ is the quenching temperature at which the emission intensity drops to 50% from its original intensity. The values of ΔE were calculated to be 0.625 and 0.485 eV for $\text{K}_3\text{YSi}_2\text{O}_7:0.04\text{Eu}$ and $\text{K}_3\text{YSi}_2\text{O}_7:0.02\text{Ce}$ phosphor, respectively, which is quite lower than that of $\text{YAG}:\text{Ce}^{3+}$ (0.81 eV).⁴⁷ Thus, both $\text{K}_3\text{YSi}_2\text{O}_7:0.04\text{Eu}$ and $\text{K}_3\text{YSi}_2\text{O}_7:0.02\text{Ce}$ phosphors show poor thermal stability. Moreover, the lowest 5d-level locations for Ce^{3+} are much closer to the conduction band than that of Eu^{2+} (Figure 4f). Therefore, it is reasonable that $\text{K}_3\text{YSi}_2\text{O}_7:0.04\text{Eu}$ has relatively better thermal stability than that of $\text{K}_3\text{YSi}_2\text{O}_7:0.02\text{Ce}$.⁴⁸ Although the $\text{K}_3\text{YSi}_2\text{O}_7:0.04\text{Eu}$ and $\text{K}_3\text{YSi}_2\text{O}_7:0.02\text{Ce}$ phosphors show poor thermal stability in this work, it may be improved in the future by phosphor coating techniques or chemical substitution strategies.

Application for WLEDs. To evaluate the potential applications for WLED lighting we constructed two different types of WLEDs (i and ii) consisting of a NUV chip ($\lambda_{\text{max}} = 395 \text{ nm}$) and a blue chip ($\lambda_{\text{max}} = 455 \text{ nm}$) encapsulated in translucent resin containing various phosphors. The PL spectra of the as-fabricated WLEDs are shown in Figure 5a–d. The WLED constructed with a mixture of $\text{K}_3\text{YSi}_2\text{O}_7:0.02\text{Ce}$ and $\text{K}_3\text{YSi}_2\text{O}_7:0.04\text{Eu}$ (mass ratio, 1:1.2) exhibits CIE color coordinates of ($x = 0.3615$, $y = 0.3713$) with low CCT (4523 K) and high R_a (90.1) at a forward bias current of 20 mA (Figure 5a). The WLED prepared with a blue chip coupled with $\text{Ba}_2\text{SiO}_4:\text{Eu}$ and $\text{K}_3\text{YSi}_2\text{O}_7:0.04\text{Eu}$ phosphors with the mass ratio 1:3.2 (Figure 5c) shows CIE color

coordinates of ($x = 0.3332$, $y = 0.3331$) with CCT of 5462 K and R_a of 90.4 at a forward bias current of 20 mA. The CCT value of the fabricated WLED can be further optimized by increasing the amount of red phosphor $\text{K}_3\text{YSi}_2\text{O}_7:\text{Eu}$. The PL spectra of two WLEDs devices are also measured under different forward bias currents (20–160 mA) and are shown in Figure 5b and 5d, and the specific optical parameters are given in Table S6. The emission colors of fabricated WLEDs move to warm light with increasing currents (Figure 5e), which is due to enhancement of green and red emission. Figure 5f displays the photographs of two different types of WLEDs packaged with different mass ratios of phosphors. For the first WLEDs system (from i-1 to i-8), the mass ratio of $\text{K}_3\text{YSi}_2\text{O}_7:0.02\text{Ce}$ and $\text{K}_3\text{YSi}_2\text{O}_7:0.04\text{Eu}$ gradually increased from 1:0.9 to 1:1.6, and the mass ratio of $\text{Ba}_2\text{SiO}_4:\text{Eu}$ and $\text{K}_3\text{YSi}_2\text{O}_7:0.04\text{Eu}$ gradually changed from 1:2.8 to 1:3.5 in the second WLEDs system (from ii-1 to ii-8). These results indicate that $\text{K}_3\text{YSi}_2\text{O}_7:\text{Eu}$ could be considered as an excellent candidate for application in blue or NUV WLEDs.

CONCLUSIONS

In summary, Eu/Ce -doped $\text{K}_3\text{YSi}_2\text{O}_7$ phosphors with multi-color emission have been reported, suggesting substantial scientific progress and unveiling the limitations of oxide phosphors especially pumped by blue light. Their luminescence properties are directly related to the local environment of the activators, and the paramount understanding the crystallographic site occupation is discussed via a combined experimental and theoretical method. Under 450 nm blue light excitation, $\text{K}_3\text{YSi}_2\text{O}_7:\text{Eu}$ shows an orange-red emission with the coexistence of Eu^{2+} and Eu^{3+} in a single host. $\text{K}_3\text{YSi}_2\text{O}_7:\text{Ce}$ shows green luminescence peaking at approximately 514 nm when excited by 394 nm NUV light. Crystal structure investigation via experiments as well as DFT calculations have found that Eu^{3+} and Ce^{3+} occupy a Y2 crystallographic site and Eu^{2+} occupies both K1 and Y2 sites in $\text{K}_3\text{YSi}_2\text{O}_7$ host. The small PBE band gap (3.69 eV) of $\text{K}_3\text{YSi}_2\text{O}_7$ host and the selective occupation of Eu^{2+} in K1 and Y2 sites leads to a broad emission in the orange-red region. The encapsulated WLEDs based on the $\text{K}_3\text{YSi}_2\text{O}_7:\text{Eu}$, $\text{K}_3\text{YSi}_2\text{O}_7:\text{Ce}$, and $\text{Ba}_2\text{SiO}_4:\text{Eu}$ phosphors show high color-rendering index ($R_a = 90.1$, 90.4), indicating that the new $\text{K}_3\text{YSi}_2\text{O}_7:\text{Eu}/\text{Ce}$ phosphors can be candidates for low-cost WLED with high color rendering index. This finding on the luminescence of (Eu^{2+} , Ce^{3+} , and Eu^{3+})-doped inorganic solids depending on the occupied crystallographic sites in the lattice can enable substantial discovery of new blue light and NUV light pumped oxide-based phosphors for white LEDs.

ASSOCIATED CONTENT

Supporting Information

The Supporting Information is available free of charge on the ACS Publications website at DOI: 10.1021/acs.chemmater.9b02990.

Main parameters of processing and refinement; fractional atomic coordinates and isotropic displacement parameters; main bond lengths; detailed investigation of Y, K cations local environment; luminescent decay times and percentage contributions; optical parameters of as-fabricated WLEDs; Rietveld refinement results; PLE and PL spectra; Gaussian fitting curves and room-temperature decay and fitting curves (PDF)

■ AUTHOR INFORMATION

Corresponding Authors

*E-mail: ongspong@eng.ucsd.edu.

*E-mail: xiazg@scut.edu.cn.

ORCID 

Shyue Ping Ong: 0000-0001-5726-2587

Qinyuan Zhang: 0000-0001-6544-4735

Zhiguo Xia: 0000-0002-9670-3223

Author Contributions

§J.Q. and M.A.: These authors contribute equally to this work.

Notes

The authors declare no competing financial interest.

■ ACKNOWLEDGMENTS

This work was supported by the National Natural Science Foundation of China (Nos. 51722202, 51972118 and 51572023), Natural Science Foundations of Beijing (2172036), Fundamental Research Funds for the Central Universities (FRF-TP-18-002C1), and Guangdong Provincial Science & Technology Project (2018A050506004). This work was also supported by the National Science Foundation, Ceramics Program (No. 1911372), and the computational resources were provided by the Extreme Science and Engineering Discovery Environment (XSEDE) supported by the National Science Foundation (No. ACI-1548562).

■ REFERENCES

(1) Xia, Z.; Liu, Q. Progress in discovery and structural design of color conversion phosphors for LEDs. *Prog. Mater. Sci.* **2016**, *84*, 59–117.

(2) Li, G.; Tian, Y.; Zhao, Y.; Lin, J. Recent progress in luminescence tuning of Ce³⁺ and Eu²⁺-activated phosphors for pc-WLEDs. *Chem. Soc. Rev.* **2015**, *44*, 8688–8713.

(3) Wei, Y.; Xing, G.; Liu, K.; Li, G.; Dang, P.; Liang, S.; Liu, M.; Cheng, Z.; Jin, D.; Lin, J. New strategy for designing orangish-red-emitting phosphor via oxygen-vacancy-induced electronic localization. *Light Sci. Appl.* **2019**, *8*, 15.

(4) Qiao, J.; Ning, L.; Molokeev, M. S.; Chuang, Y. C.; Liu, Q.; Xia, Z. Eu²⁺ Site Preferences in the Mixed Cation K₂BaCa(PO₄)₂ and Thermally Stable Luminescence. *J. Am. Chem. Soc.* **2018**, *140*, 9730–9736.

(5) Zhao, M.; Liao, H.; Molokeev, M. S.; Zhou, Y.; Zhang, Q.; Liu, Q.; Xia, Z. Emerging ultra-narrow-band cyan-emitting phosphor for white LEDs with enhanced color rendition. *Light Sci. Appl.* **2019**, *8*, 38.

(6) Zhang, Z.; Ma, C.; Gautier, R.; Molokeev, M. S.; Liu, Q.; Xia, Z. Structural Confinement toward Giant Enhancement of Red Emission in Mn²⁺-Based Phosphors. *Adv. Funct. Mater.* **2018**, *28*, 1804150.

(7) Jang, H. S.; Won, Y. H.; Jeon, D. Y. Improvement of electroluminescent property of blue LED coated with highly luminescent yellow-emitting phosphors. *Appl. Phys. B: Lasers Opt.* **2009**, *95*, 715–720.

(8) Bachmann, V.; Ronda, C.; Meijerink, A. Temperature quenching of yellow Ce³⁺ luminescence in YAG: Ce. *Chem. Mater.* **2009**, *21*, 2077–2084.

(9) Wang, Z.; Ha, J.; Kim, Y. H.; Im, W. B.; McKittrick, J.; Ong, S. P. Mining Unexplored Chemistries for Phosphors for High-Color-Quality White-Light-Emitting Diodes. *Joule* **2018**, *2*, 914–926.

(10) Pust, P.; Weiler, V.; Hecht, C.; Tucks, A.; Wochnik, A. S.; Henss, A. K.; Wiechert, D.; Scheu, C.; Schmidt, P. J.; Schnick, W. Narrow-band red-emitting Sr[LiAl₃N₄]:Eu²⁺ as a next-generation LED-phosphor material. *Nat. Mater.* **2014**, *13*, 891–896.

(11) Uheda, K.; Hirotsaki, N.; Yamamoto, H. Host lattice materials in the system Ca₃N₂-AlN-Si₃N₄ for white light emitting diode. *Phys. Status Solidi A* **2006**, *203*, 2712–2717.

(12) Xie, R.-J.; Hirotsaki, N.; Suehiro, T.; Xu, F.-F.; Mitomo, M. A simple, efficient synthetic route to Sr₂Si₅N₈:Eu²⁺-based red phosphors for white light-emitting diodes. *Chem. Mater.* **2006**, *18*, 5578–5583.

(13) Wang, L.; Xie, R. J.; Li, Y.; Wang, X.; Ma, C. G.; Luo, D.; Takeda, T.; Tsai, Y. T.; Liu, R. S.; Hirotsaki, N. Ca_{1-x}Li_xAl_{1-x}Si_{1+x}N₃:Eu²⁺ solid solutions as broadband, color-tunable and thermally robust red phosphors for superior color rendition white light-emitting diodes. *Light: Sci. Appl.* **2016**, *5*, No. e16155.

(14) Takahashi, T.; Adachi, S. Mn⁴⁺-activated red photoluminescence in K₂SiF₆ phosphor. *J. Electrochem. Soc.* **2008**, *155*, E183–E188.

(15) Setlur, A. A.; Radkov, E. V.; Henderson, C. S.; Her, J.-H.; Srivastava, A. M.; Karkada, N.; Kishore, M. S.; Kumar, N. P.; Aesram, D.; Deshpande, A. Energy-efficient, high-color-rendering LED lamps using oxyfluoride and fluoride phosphors. *Chem. Mater.* **2010**, *22*, 4076–4082.

(16) Zhu, H.; Lin, C. C.; Luo, W.; Shu, S.; Liu, Z.; Liu, Y.; Kong, J.; Ma, E.; Cao, Y.; Liu, R. S.; Chen, X. Highly efficient non-rare-earth red emitting phosphor for warm white light-emitting diodes. *Nat. Commun.* **2014**, *5*, 4312.

(17) Dorenbos, P. Relation between Eu²⁺ and Ce³⁺ f←d-transition energies in inorganic compounds. *J. Phys.: Condens. Matter* **2003**, *15*, 4797.

(18) Peng, M.; Pei, Z.; Hong, G.; Su, Q. The reduction of Eu³⁺ to Eu²⁺ in BaMgSiO₄:Eu prepared in air and the luminescence of BaMgSiO₄:Eu²⁺ phosphor. *J. Mater. Chem.* **2003**, *13*, 1202–1205.

(19) Xie, H.; Lu, J.; Guan, Y.; Huang, Y.; Wei, D.; Seo, H. J. Abnormal reduction, Eu³⁺ → Eu²⁺, and defect centers in Eu³⁺-doped polycite, CsAlSi₂O₆, prepared in an oxidizing atmosphere. *Inorg. Chem.* **2014**, *53*, 827–834.

(20) Zhang, Y.; Li, X.; Li, K.; Lian, H.; Shang, M.; Lin, J. Crystal-site engineering control for the reduction of Eu³⁺ to Eu²⁺ in CaYAlO₄: structure refinement and tunable emission properties. *ACS Appl. Mater. Interfaces* **2015**, *7*, 2715–2725.

(21) Liu, X.; Xie, W.; Lu, Y.; Feng, J.; Tang, X.; Lin, J.; Dai, Y.; Xie, Y.; Yan, L. Multichannel Luminescence Properties of Mixed-Valent Eu²⁺/Eu³⁺ Coactivated SrAl₃BO₇ Nanocrystalline Phosphors for Near-UV LEDs. *Inorg. Chem.* **2017**, *56*, 13829–13841.

(22) Xia, Z.; Ma, C.; Molokeev, M. S.; Liu, Q.; Rickert, K.; Poepplmeier, K. R. Chemical Unit Cosubstitution and Tuning of Photoluminescence in the Ca₂(Al_{1-x}Mg_x)(Al_{1-x}Si_{1+x})O₇:Eu²⁺ Phosphor. *J. Am. Chem. Soc.* **2015**, *137*, 12494–12497.

(23) Latshaw, A. M.; Morrison, G.; Loye, K. D. z.; Myers, A. R.; Smith, M. D.; Loye, H.-C. z. Intrinsic blue-white luminescence, luminescence color tunability, synthesis, structure, and polymorphism of K₃YSi₂O₇. *CrystEngComm* **2016**, *18*, 2294–2302.

(24) Gautier, R.; Li, X.; Xia, Z.; Massuyeau, F. Two-Step Design of a Single-Doped White Phosphor with High Color Rendering. *J. Am. Chem. Soc.* **2017**, *139*, 1436–1439.

(25) Sung-Ho Baek; Jeom-Oh Kim; Min-Ki Kwon; Il-Kyu Park; Seok-In Na; Ja-Yeon Kim; Bongjin Kim; Seong-Ju Park. Enhanced carrier confinement in AlInGaN-InGaN quantum wells in near ultraviolet light-emitting diodes. *IEEE Photonics Technol. Lett.* **2006**, *18*, 1276–1278.

(26) Wang, Z.; Chu, I.-H.; Zhou, F.; Ong, S. P. Electronic Structure Descriptor for the Discovery of Narrow-Band Red-Emitting Phosphors. *Chem. Mater.* **2016**, *28*, 4024–4031.

(27) Dorenbos, P. Thermal quenching of Eu²⁺ 5d-4f luminescence in inorganic compounds. *J. Phys.: Condens. Matter* **2005**, *17*, 8103.

(28) Qiao, J.; Ning, L.; Molokeev, M. S.; Chuang, Y.-C.; Zhang, Q.; Poepplmeier, K. R.; Xia, Z. Site-selective occupancy of Eu²⁺ toward blue-light excited red emission in Rb₃YSi₂O₇:Eu phosphor. *Angew. Chem., Int. Ed. Engl.* **2019**, *131*, 11645–11650.

(29) TOPAS, V.2: *General profile and structure analysis software for powder diffraction data-User's Manual*; Bruker AXS: Karlsruhe, Germany, 2008.

(30) Kresse, G.; Furthmüller, J. Efficient iterative schemes for ab initio total-energy calculations using a plane-wave basis set. *Phys. Rev. B: Condens. Matter Mater. Phys.* **1996**, *54*, 11169.

(31) Blöchl, P. E. Projector augmented-wave method. *Phys. Rev. B: Condens. Matter Mater. Phys.* **1994**, *50*, 17953.

(32) Jain, A.; Ong, S. P.; Hautier, G.; Chen, W.; Richards, W. D.; Dacek, S.; Cholia, S.; Gunter, D.; Skinner, D.; Ceder, G. Commentary: The Materials Project: A materials genome approach to accelerating materials innovation. *APL Mater.* **2013**, *1*, 011002.

(33) Ong, S. P.; Richards, W. D.; Jain, A.; Hautier, G.; Kocher, M.; Cholia, S.; Gunter, D.; Chevrier, V. L.; Persson, K. A.; Ceder, G. Python Materials Genomics (pymatgen): A robust, open-source python library for materials analysis. *Comput. Mater. Sci.* **2013**, *68*, 314–319.

(34) Dudarev, S.; Botton, G.; Savrasov, S.; Humphreys, C.; Sutton, A. Electron-energy-loss spectra and the structural stability of nickel oxide: An LSDA+ U study. *Phys. Rev. B: Condens. Matter Mater. Phys.* **1998**, *57*, 1505.

(35) Wei, S.-H.; Zhang, S. Chemical trends of defect formation and doping limit in II-VI semiconductors: The case of CdTe. *Phys. Rev. B: Condens. Matter Mater. Phys.* **2002**, *66*, 155211.

(36) Waroquiers, D.; Gonze, X.; Rignanese, G.-M.; Welker-Nieuwoudt, C.; Rosowski, F.; Göbel, M.; Schenk, S.; Degelmann, P.; André, R.; Glaum, R. Statistical analysis of coordination environments in oxides. *Chem. Mater.* **2017**, *29*, 8346–8360.

(37) Hoppe, R. The coordination number—an “inorganic chameleon”. *Angew. Chem., Int. Ed. Engl.* **1970**, *9*, 25–34.

(38) Zhao, M.; Xia, Z.; Huang, X.; Ning, L.; Gautier, R.; Molokeev, M. S.; Zhou, Y.; Chuang, Y.-C.; Zhang, Q.; Liu, Q. Li substituent tuning of LED phosphors with enhanced efficiency, tunable photoluminescence, and improved thermal stability. *Sci. Adv.* **2019**, *5*, No. eaav0363.

(39) Li, S.; Wang, L.; Tang, D.; Cho, Y.; Liu, X.; Zhou, X.; Lu, L.; Zhang, L.; Takeda, T.; Hirosaki, N.; Xie, R.-J. Achieving High Quantum Efficiency Narrow-Band β -Sialon:Eu²⁺ Phosphors for High-Brightness LCD Backlights by Reducing the Eu³⁺ Luminescence Killer. *Chem. Mater.* **2018**, *30*, 494–505.

(40) Henderson, B.; Imbusch, G. F. *Optical spectroscopy of inorganic solids*; Oxford University Press: 2006; Vol. 44.

(41) Jang, H. S.; Im, W. B.; Lee, D. C.; Jeon, D. Y.; Kim, S. S. Enhancement of red spectral emission intensity of Y₃Al₅O₁₂:Ce³⁺ phosphor via Pr co-doping and Tb substitution for the application to white LEDs. *J. Lumin.* **2007**, *126*, 371–377.

(42) Blasse, G.; Grabmaier, B. How Does a Luminescent Material Absorb Its Excitation Energy? *Luminescent Materials*; Springer, 1994; pp 10–32.

(43) Burns, R. G.; Burns, R. G. *Mineralogical applications of crystal field theory*; Cambridge University Press, 1993; Vol. 5.

(44) Qiao, J.; Zhao, J.; Liu, Q.; Xia, Z. Recent advances in solid-state LED phosphors with thermally stable luminescence. *J. Rare Earths* **2019**, *37*, 565–572.

(45) Shionoya, S.; Yen, W. M.; Yamamoto, H. *Phosphor handbook*; CRC Press, 2018.

(46) Ning, L.; Ji, X.; Dong, Y.; Jin, W.; Huang, Y.; Pan, Z.; Tanner, P. A. First-principles study of Ce-doped Y₃Al₅O₁₂ with Si-N incorporation: electronic structures and optical properties. *J. Mater. Chem. C* **2016**, *4*, S214–S221.

(47) Ueda, J.; Dorenbos, P.; Bos, A. J. J.; Meijerink, A.; Tanabe, S. Insight into the Thermal Quenching Mechanism for Y₃Al₅O₁₂:Ce³⁺ through Thermoluminescence Excitation Spectroscopy. *J. Phys. Chem. C* **2015**, *119*, 25003–25008.

(48) Dorenbos, P. Energy of the Eu²⁺ 5d state relative to the conduction band in compounds. *J. Lumin.* **2008**, *128*, 578–582.